Error analysis of 3D shearography using finite-element modelling

D. T. Goto[a, b], R.M. Groves[a]
[a]Delft University of Technology, Optical Non-Destructive Testing Laboratory, Faculty of Aerospace Engineering, Kluyverweg 1, 2600 GB Delft, The Netherlands
[b]Universidade Federal de Santa Catarina, Laboratório de Metrologia e Automatização, Departamento de Engenharia Mecânica, CEP 88040-970, Florianópolis, Brazil

ABSTRACT

This paper describes the development of an opto-mechanical simulation of a complete shearography system, including the shearography instrument, the samples and the test environment. This simulation is applied to the measurement of 3D strains in engineering samples. The samples are a cylinder loaded by internal pressure and a flat plate under axial load. Finite elements models are used to obtain the displacements fields. A 3D shearography instrument consisting of a laser and four cameras has been simulated using the optical model. Combining the finite elements and optical simulations allows phase maps to be generated, which are the predictions for measurements using the complete test setup. Errors due to sample material properties, loading inaccuracy and dimensional tolerances are included in the model and this allows the calculation of phase maps at the minimum and maximum error limits. The simulation through path lengths and the simulation by inverted shearography processing provide similar results and the difference is associated with the approximation introduced by the sensitivity vector.

Keywords: 3D Shearography, strain measurement, finite element model, error analysis.

1. INTRODUCTION

Shearography[1] is a speckle shearing interferometry technique capable of measuring surface displacement gradient, from which strain information can be extracted. Shearography is commonly used for non-destructive testing applications in high technology industries[2]. A typical modern shearography instrument is composed of a laser, an interferometer incorporating phase shifting, a digital camera and a computer for data processing, including phase extraction, filtering, and the calculation and display of displacement gradient fields. The 3D configuration of shearography can be used for quantitative 3D strain measurement, however to achieve this, effort is required to compensate for errors, ideally automatically in the instrument processing software.

Errors due to the illumination and imaging geometry are related to the sensitivity vector of the system. The sensitivity vector is defined as the bisector of the illumination and observation directions and, in general, a constant sensitivity vector is adopted. However the use of an expanded laser beam[3,4] and the finite size of the object as well as the camera sensor[5], introduces variable illumination and observation vectors and as a result, variable sensitivity vectors are inherent to the system. Errors are also associated with the magnitude of the shear. An accurate measurement of the shear distance is difficult to perform and in most cases a known distance at the object surface is used[6]. As an alternative, digital image correlation may be used[7]. The shear magnitude may also be variable along the surface due to object curvature[8] or because of the Michelson interferometer[9]. At the data processing level, errors may be introduced, for example, by filtering processes[10]. For 3D shearography, extra error sources are linked with matrix transformation operations[8,11] and with the misalignment of the camera's sensor plane with the object surface, which requires extra steps during processing for image dewarping and co-registration[11]. In this case, the dewarping algorithm also provides a method to obtain the observation vectors[11].

In order to calibrate a shearography instrument with multiple cameras and one laser source, a combination of finite element (FE) simulations and optical simulations have been used, which can subsequently be used to compare with an experimental instrument and test set-up, see figure 1. In this paper, two simulation methods for the opto-mechanical simulation have been identified and the strain and maps of phase change calculated by these methods are compared. Errors due to the uncertainty in Young's modulus and Poisson's ratio of the sample material, manufacturing tolerances and loading inaccuracy were simulated in the model and their effects on the phase maps are calculated. Also the uncertainty introduced by sensitivity vectors approximations is discussed.

Optical Micro- and Nanometrology III, edited by Christophe Gorecki, Anand Krishna Asundi, Wolfgang Osten,
Proc. of SPIE Vol. 7718, 771816 · © 2010 SPIE · CCC code: 0277-786X/10/$18 · doi: 10.1117/12.853602

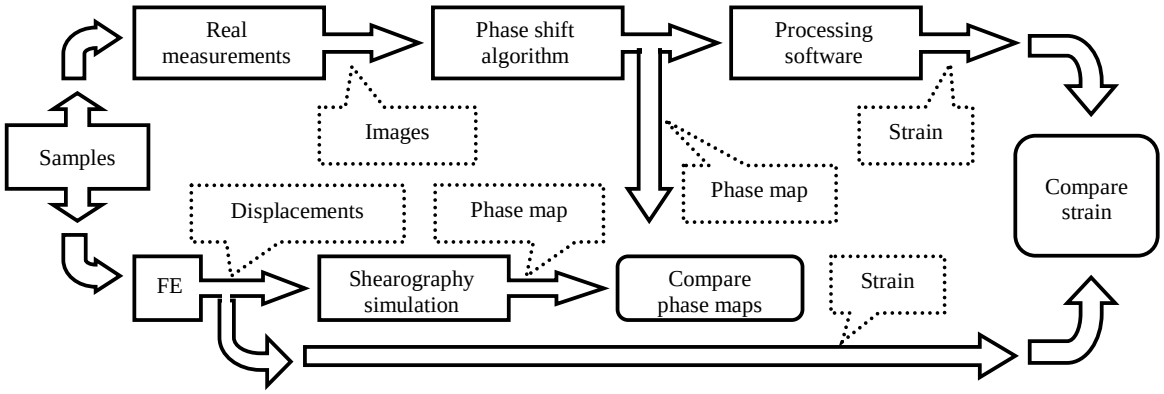

Figure 1. Shearography instrument calibration strategy.

2. SHEAROGRAPHY THEORY

Shearography is a measurement technique based on the interference of light. The object being measured is illuminated by an expanded laser beam and light scattered from the object surface is recorded by a digital camera. A shearing Michelson interferometer is placed in front of the camera and adjusted so that each pixel on the camera sensor receives light from two different points on the object surface. These two points are separated by the shear distance. The result is a double image, where the intensity of light at each pixel contains information related to the difference in the phase of the light rays from those two points. This image is known as interferogram. Mathematically, the intensity at each pixel in the interferogram is described by[1]:

$$I = 2I_o(1+\gamma\cos\phi) \tag{1}$$

Where $I_o = (a_1^2 + a_2^2)/2$, $\gamma = 2a_1a_2/(a_1^2 + a_2^2)$, a_1 and a_2 are the amplitudes of the light rays from points P_1 and P_2 on the object surface and ϕ is the difference of phase between these two points.

To perform a measurement, reference interferograms are recorded and a phase shift algorithm[12] is applied to determine the difference of phase at each pixel. This forms the reference map of difference of phase. The object is then loaded to a second state, further interferograms are recorded and the phase shift algorithm is again used to determine the map of difference of phase at this second loading state. This is the signal map of difference of phase. Reference and signal maps are then correlated by subtraction to yield an image with fringes. This image is referred to as phase map ($\Delta\phi$). From the optics point of view, the phase of a light ray is associated with the light path between the laser source (S), a point on the object (for example P_1) and the camera sensor (C), according to the figure below.

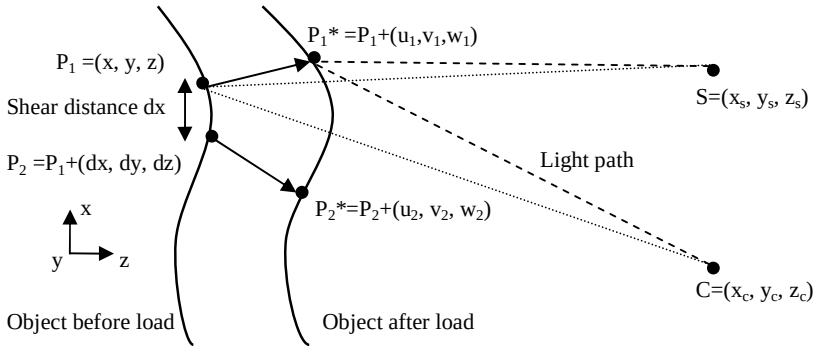

Figure 2. Schematic of the optical and engineering mechanics interpretation of the phase change.

The phase map is then described by[1]:

$$\Delta\phi = \frac{2\pi}{\lambda}\left[\left(\overline{SP_1^*C} - \overline{SP_1C}\right) - \left(\overline{SP_2^*C} - \overline{SP_2C}\right)\right] = \frac{2\pi}{\lambda}\left[d_{path1} - d_{path2}\right] \tag{2}$$

Still considering Figure 1, the engineering mechanics interpretation of the map of phase map may be obtained as:

$$\Delta\phi = \frac{2\pi}{\lambda}\vec{k}\cdot\begin{bmatrix} u_2 - u_1 \\ v_2 - v_1 \\ w_2 - w_1 \end{bmatrix} \cong \frac{2\pi}{\lambda}\vec{k}\cdot\begin{bmatrix} \partial u/\partial x \\ \partial v/\partial x \\ \partial w/\partial x \end{bmatrix}\cdot dx \tag{3}$$

Where dx is the shear distance. The equation may also be formed with the shear in y direction and in this case the displacement gradients are along y direction. The vector $\vec{k}$ is known as sensitivity vector and is approximated by:

$$\vec{k} = \frac{\overrightarrow{P_1S}}{\left|\overrightarrow{P_1S}\right|} + \frac{\overrightarrow{P_1C}}{\left|\overrightarrow{P_1C}\right|} \tag{4}$$

A 3D shearography system with three cameras is capable of generating three maps of phase difference for each shearing direction, which allows isolation of each displacement gradient by solving a coordinate transformation[5]:

$$\begin{bmatrix} \partial u/\partial x \\ \partial v/\partial x \\ \partial w/\partial x \end{bmatrix} = \frac{\lambda}{2\pi}\begin{bmatrix} \vec{k}_{cam1} \\ \vec{k}_{cam2} \\ \vec{k}_{cam3} \end{bmatrix}^{-1}\begin{bmatrix} \Delta\phi_{x,cam1} \\ \Delta\phi_{x,cam2} \\ \Delta\phi_{x,cam3} \end{bmatrix}\frac{1}{dx} = \frac{\lambda}{2\pi}M^{-1}\begin{bmatrix} \Delta\phi_{x,cam1} \\ \Delta\phi_{x,cam2} \\ \Delta\phi_{x,cam3} \end{bmatrix}\frac{1}{dx} \tag{5}$$

M is 3x3 matrix defined by concatenating the components of the sensitivity vector for each camera.

3. EXPERIMENTAL DETAILS OF THE SYSTEM BEING MODELLED

3.1 Shearography instrument

The shearography system is composed of four cameras and one laser source. The interferometers are positioned at the tips of a cross and the laser source is placed just below the center of the cross as indicated by the figure below.

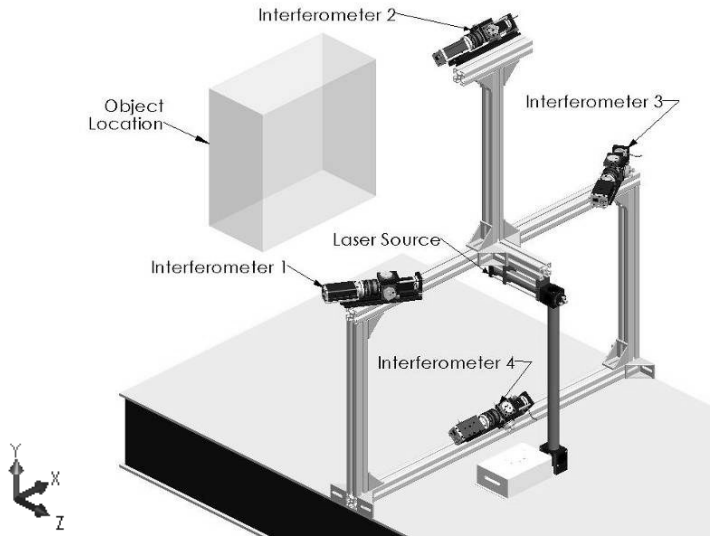

Figure 3. 3D Shearography instrument, showing the locations of the laser and the interferometers.

These camera positions were considered to minimize errors in the matrix transformation on equation (5)[13]. A large viewing angle is desirable to minimize errors in the coordinate transformation. On the other hand, the area on the object covered by one pixel on the camera increases, is spatially distorted and a lower light intensity reaches the camera. These effects cause a loss of spatial resolution and increase the uncertainty and the minimum limit for the shear distance. For large working distance, the error in the sensitivity vector reduces[1]. The distance between the object and the shearography instrument in the modeled system is 800mm. The structure is about 1m in length (x direction) and 1m in height (y direction). Although three cameras are enough to characterize all components of in plane strain, one extra camera allows multiple measurement channels combinations at equation (5) and a better confidence level is then obtained[14].

3.2 Calibration Samples

Two calibration samples were designed and manufactured. One is based on a cylinder, loaded by internal pressure, and the other is a flat plate loaded axially.

One special focus is the measurement of curved surfaces, thus the first sample is a thin wall aluminum cylinder of length 400mm, external diameter of 190mm and wall thickness of 5mm manufactured by rolling a plate and welding the seam. Aluminum end caps were welded to the cylinder. Oil is pumped into the cylinder by a mechanical pump and the loading magnitude is controlled by a pressure gauge.

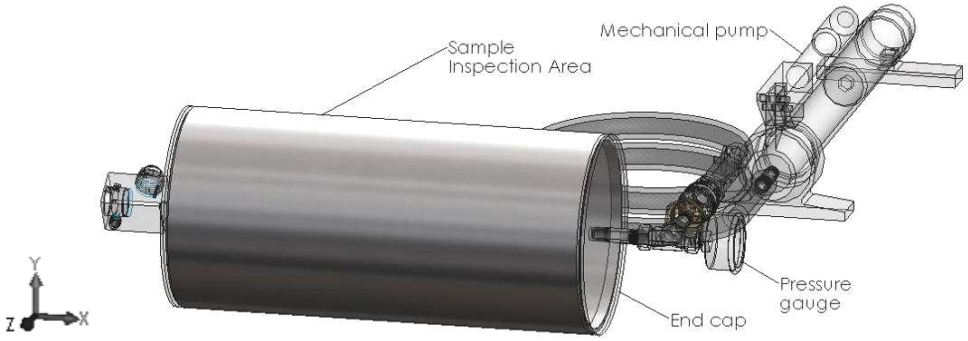

Figure 4. Cylinder calibration sample.

The equations (adapted from the thick wall model[15]) for longitudinal and tangential strains are respectively:

$$\varepsilon_l = \frac{r_i^2}{r_o^2 - r_i^2} \cdot \frac{(1-2\upsilon)P}{E} \tag{6}$$

$$\varepsilon_t = \frac{r_i^2}{r_o^2 - r_i^2} \cdot \frac{(2-\upsilon)P}{E} \tag{7}$$

Where r_i and r_o the internal and external radius. P is the internal pressure and E the elastic modulus. As observed by the equations, the uncertainty in the material properties (elastic modulus and Poisson's ratio) has a strong influence in the strain. Also, curved surfaces are more challenging for the optical simulation, because of errors due to shear magnitude variation[8].

A flat sample is also desirable as a calibration sample, since the shear variation across the object surface is minimized. The displacement may also be directly controlled, which eliminates errors due to Young's modulus uncertainty and sample thickness tolerances. For these reasons, as second sample, a flat plate 300 by 150 by 1 mm was manufactured from an aluminum sheet (2024 T3). A steel structure with a lever system is used to apply loading to the sample. The sample is attached to one of the arms of the lever and by controlling the angle between the lever arms, it is possible to control the displacement on the sample directly. Such design allows accurate loading control, although, the loading is not perfectly axial due to the lever system. This calibration sample is shown in Figure 5.

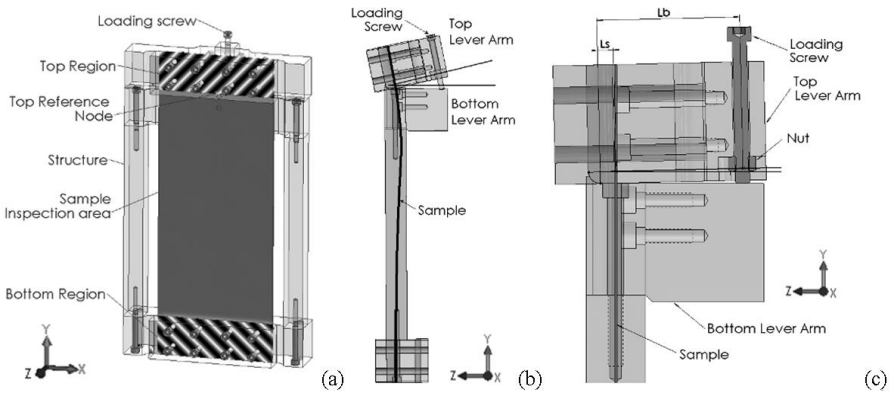

Figure 5. (a) Plate sample attached to the loading structure. (b) Side view demonstrating the loading condition and (c) the detail of the lever system.

Using an analytical approach, the strains along the y direction (ε_{22}) and x direction (ε_{11}) can be calculated as:

$$\varepsilon_{22} = \frac{1}{l_o} \cdot \frac{l_s}{l_b} \cdot \theta p \tag{8}$$

$$\varepsilon_{11} = -\upsilon \varepsilon_{22} = -\upsilon \frac{1}{l_o} \cdot \frac{l_s}{l_b} \cdot \theta p \tag{9}$$

where l_o is the sample height, l_b is distance between the support point and the loading screw, l_s is the distance between the support point and the sample, θ is the loading screw turning angle, p is the loading screw pitch and ν is Poisson's ratio. Using the analytical equations the parameters that influence strain distribution may be identified and the combination that generates the minimum and maximum strains may be determined. The following uncertainties were considered:

Table 1. Considered uncertainties for input in the FE model and expected strains according to analytical model.

Plate sample				Cylinder sample			
	Min error	Nominal	Max error		Min error	Nominal	Max error
Elastic modulus	72,4GPa	72,4Pa	72,4GPa	Elastic modulus	73,14MPa	69MPa	64,86MPa
Poisson's ratio	0,3234	0,3300	0,3366	Poisson's ratio	0,3234	0.3300	0,3366
Height	298,5mm	297mm	295,5mm	External radius	95,11mm	95mm	94,89mm
Loading screw angle	3,725turns	3,850turns	3.975 turns	Internal radius	89,89mm	90mm	90,11mm
Lever sample arm	5,17mm	5,5mm	5,85mm	Pressure	4,28MPa	4,50MPa	4,72MPa
Lever screw arm	61,0mm	60mm	59,0mm				
				Analytical strain			
Analytical strain				Radial	$-4{,}75\cdot10^{-4}$	$-5{,}65\cdot10^{-4}$	$-6{,}74\cdot10^{-4}$
Longitudinal ε_{22}	$1{,}28\cdot10^{-3}$	$1{,}43\cdot10^{-3}$	$1{,}59\cdot10^{-4}$	Longitudinal	$1{,}73\cdot10^{-4}$	$1{,}94\cdot10^{-4}$	$2{,}18\cdot10^{-4}$
Transversal ε_{11}	$-4{,}13\cdot10^{-4}$	$-4{,}72\cdot10^{-4}$	$-5{,}36\cdot10^{-4}$	Tangential	$8{,}21\cdot10^{-4}$	$9{,}54\cdot10^{-4}$	$1{,}11\cdot10^{-3}$

4. SIMULATIONS

4.1 Finite element models

Finite element simulations of both samples were performed using Abaqus (version 6.8) on a Pentium D 3,40GHz with 2GB of RAM. For the cylinder sample, a 2D model consisting of one quarter of the cylinder was prepared with adequate symmetry boundary conditions (axial degree of freedom normal to the cutting plane and in-plane rotational degrees of freedom set to zero). The mesh density in the cylindrical surface was selected to approximate the shearography instrument camera resolution (2456 pixels on the horizontal direction). It is desirable to use one node on the FE model for each pixel on the camera. In this way the phase maps from the shearography computational model have the same resolution of phase maps from the experimental shearography instrument. In summary a mesh with 0,17mm between consecutive nodes was used, with 31 nodes used along the thickness.

The plate sample was divided into three components for the simulation, see figure 5. The regions where the sample is in contact with the structure (top and bottom regions) were defined as rigid body (relative displacement of nodes within the region is zero). All degrees of freedom of the bottom region were set to zero. A CAD model of the lever system was used to determine the axial (along y direction) and rotational (along x direction) displacements of the top region. Uncertainties on the lever arms lengths (L_b and L_s) were included in the CAD model and transferred to uncertainties on the top region displacements. The inspection area is the central region of the sample. Although 2056 nodes are desirable along the vertical direction in this region (to match camera resolution), only 515 nodes were used due to computational limitations. This FE model has one node for every 4 pixels on the camera.

4.2 Shearography simulation - Path length method

The phase map from this 3D shearography simulation is a 2D array where each element is a number in the range [0, 255], representing phase differences in the range [0, 2π]. Two methods were used to obtain such map. The first approach is derived from shearography theory, and is based on path length variation. The basic sequence of tasks for the simulation is: 1. Read displacements from the FE model output file and organize the data into a 2D array; 2. Calculate the coordinates of the nodes along the inspection surface (before loading); 3. Calculate the coordinates of the nodes after loading; 4. Read shear, laser wavelength and positions of the laser source and cameras into the simulation; 5. Calculate differences of path lengths; 6. Calculate the unwrapped phase map; 7. Calculate the wrapped phase map and 8. Rescale to 8bit range [0, 255].

A global coordinate system was defined as indicated in figure 6. A squared mesh with nodes aligned in the x and y directions is positioned along the xy plane and projected onto the object surface. Coordinates of the projected nodes are then calculated and each Cartesian component is stored in a separated 2D array referred to in this paper as $P_x(i,j)$, $P_y(i,j)$ and $P_z(i,j)$, where i and j are row and column indexes.

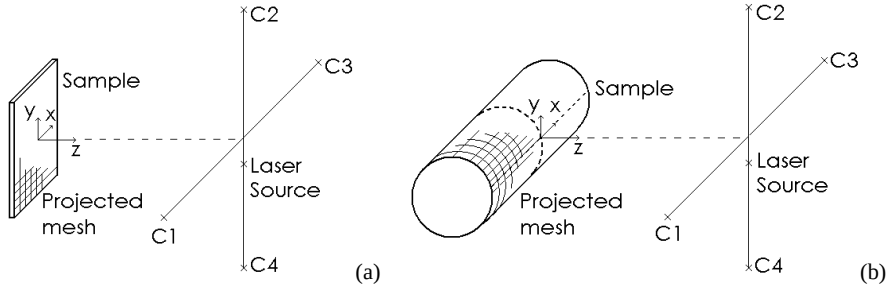

Figure 6. Adopted global coordinate system is with z direction aligned with the surface normal at the center of the object. C1, C2, C3 and C4 are the positions of the cameras.

The FE simulation for the plate sample provides displacements vectors of these projected nodes. In the case of the cylinder sample, displacement vectors are in a cylindrical coordinate system which has an axis that coincides with axis of the cylinder (u_l, u_r and u_t are the longitudinal, radial and tangential displacements, respectively). A rotation, described by equation (10), is performed to obtain displacement vectors along the global Cartesian coordinate system (u, v and w are the displacement along x, y and z direction respectively). The displacement components calculated were stored in separate 2D arrays.

$$\begin{pmatrix} u(i,j) \\ v(i,j) \\ w(i,j) \end{pmatrix} = \begin{pmatrix} 1 & 0 & 0 \\ 0 & \cos\left[\arcsin\left(P_y(i,j)/r_o\right)\right] & \sin\left[\arcsin\left(P_y(i,j)/r_o\right)\right] \\ 0 & -\sin\left[\arcsin\left(P_y(i,j)/r_o\right)\right] & \cos\left[\arcsin\left(P_y(i,j)/r_o\right)\right] \end{pmatrix} \cdot \begin{pmatrix} u_l(j) \\ u_t(j) \\ u_r(j) \end{pmatrix} \tag{10}$$

where r_o is the cylinder external radius.

2D arrays containing coordinates of nodes after loading are obtained by adding the coordinates before loading to the displacement components. Equation (11) is the example for the x coordinate and similar equations can be determined for the other components.

$$P_x^*(i,j) = P_x(i,j) + u(i,j) \tag{11}$$

The arrays of path length differences for each camera are calculated using the source ($\vec{S}$) and the camera position ($\vec{C}_{cam}$)

$$d_{path}(i,j)\Big|_{cam} = \left[\left|\overrightarrow{P^*}(i,j)-\vec{S}\right|+\left|\vec{C}_{cam}-\overrightarrow{P^*}\right|\right]-\left[\left|\vec{P}(i,j)-\vec{S}\right|+\left|\vec{C}_{cam}-\vec{P}(i,j)\right|\right] \tag{12}$$

$\overrightarrow{P^*}(i,j)$ is the position of the node after loading $\left(P_x^*(i,j),P_y^*(i,j),P_z^*(i,j)\right)$ and $\vec{P}(i,j)$ is the original position of the node $\left(P_x(i,j),P_y(i,j),P_z(i,j)\right)$.

The shear effect optically mixes points P_1 with points P_2[6], see figure 1. Points P_2 represent the image that is fixed and points P_1 represent the image that moves as one of the mirrors inside the interferometer is tilted[16]. The input variable called shear is an integer number responsible for selecting the nodes that will be correlated.

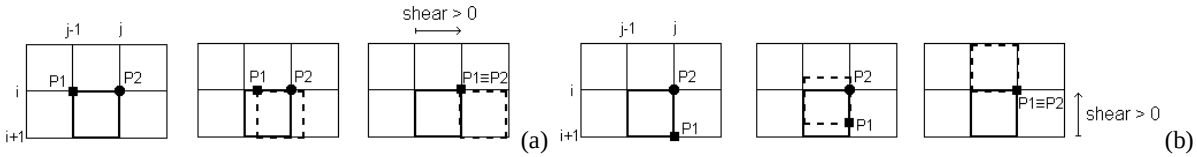

Figure 7. Shear direction convention, (a) for x direction and (b) for y direction.

Using the above convention, for shear in the x direction, the phase map described by equation (2) becomes:

$$\Delta\phi(i,j)\Big|_{cam,x} = \frac{2\pi}{\lambda}\left[d_{path1}-d_{path2}\right] = \frac{2\pi}{\lambda}\left[d_{path}(i,j-shear)\Big|_{cam}-d_{path}(i,j)\Big|_{cam}\right] \tag{13}$$

And for shear along y direction it becomes:

$$\Delta\phi(i,j)\Big|_{cam,y} = \frac{2\pi}{\lambda}\left[d_{path1}-d_{path2}\right] = \frac{2\pi}{\lambda}\left[d_{path}(i+shear,j)\Big|_{cam}-d_{path}(i,j)\Big|_{cam}\right] \tag{14}$$

On the edges of the sample, the algorithm tries to correlate points outside the sample, so the phase change is arbitrarily set to zero at these points.

To obtain the wrapped phase map, the phase at each point should be shifted a certain value (a multiple of 2π). This is implemented by:

$$\Delta\phi_{wrapped}(i,j)\Big|_{cam,shear} = \Delta\phi(i,j)\Big|_{cam,shear} - n\cdot\Delta\phi(i,j)\Big|_{cam,shear} \tag{15}$$

where *n* is obtained by dividing the phase map array (element wise) by 2π and then rounding the result to the nearest smaller integer. The last step is to rescale the wrapped phase map from the interval $[0,2\pi]$ to [0,255] by linear interpolation.

4.3 Shearography simulation – inverse shearography software method

The second approach follows closely the shearography instrument processing software, but in the opposite direction. This algorithms basic sequence of tasks is: 1. Read displacements from the FE model output file and organize the data into a 2D array; 2. Read displacements from the FE model output file and organize data into a 2D array; 3. Calculate the coordinates of nodes along the inspection surface (before loading); 4. Read the shear, laser wavelength and positions of the laser source and cameras into the simulation; 5. Calculate displacement gradients; 6. Calculate sensitivity vectors; 7. Calculate the unwrapped phase map; 8. Calculate the wrapped phase map and 9. Rescale to 8bit range [0,255].

Arrays of displacements and nodal coordinates are calculated exactly in the same way used for the path length method.

2D arrays containing displacement gradient are calculated using the displacement arrays and the actual shear distance (x_{shear} and y_{shear}). Equation (16) is for the displacement gradient along x direction:

$$\frac{\partial u}{\partial x}(i,j) = \frac{u(i,j)-u(i,j-shear)}{x_{shear}} \tag{16}$$

And for the gradient along the y direction:

$$\frac{\partial u}{\partial y}(i,j) = \frac{u(i,j) - u(i+shear,j)}{y_{shear}} \tag{17}$$

The input variable *shear* is responsible for selecting the points that will be used for the displacement gradient calculation. The actual shear distance is a multiple of the distance between consecutive nodes. As example for x shear:

$$x_{shear} = shear \cdot \left(\frac{L}{N-1} \right) \tag{18}$$

The part between parentheses is the distance between consecutive nodes, obtained using the sample total length (L) and the total number of nodes along the x direction (N). For shear in y direction, the diameter (for the cylinder) and the sample height (for the plate sample) should be used in place of L as well as the total number of nodes along y direction. The shear convention is the same as adopted for the previous method.

The Laser position ($\vec{S}$) and camera position ($\vec{C}_{cam}$) are defined as for the Path length method. The sensitivity vectors are described by equation (4) and are calculated for each camera and for shear in x direction using:

$$\vec{k}(i,j)\Big|_{cam,x} = \frac{\overrightarrow{P_1S}}{\left|\overrightarrow{P_1S}\right|} + \frac{\overrightarrow{P_1C}}{\left|\overrightarrow{P_1C}\right|} = \frac{\vec{S} - \vec{P}(i,j-shear)}{\left|\vec{S} - \vec{P}(i,j-shear)\right|} + \frac{\vec{C}_{cam} - \vec{P}(i,j-shear)}{\left|\vec{C}_{cam} - \vec{P}(i,j-shear)\right|} \tag{19}$$

where $\vec{P}(i,j-shear)$ is the original position of the node $\left(P_x(i,j-shear), P_y(i,j-shear), P_z(i,j-shear)\right)$.

For shear in the y direction, the sensitivity vector is:

$$\vec{k}(i,j)\Big|_{cam,y} = \frac{\overrightarrow{P_1S}}{\left|\overrightarrow{P_1S}\right|} + \frac{\overrightarrow{P_1C}}{\left|\overrightarrow{P_1C}\right|} = \frac{\vec{S} - \vec{P}(i+shear,j)}{\left|\vec{S} - \vec{P}(i+shear,j)\right|} + \frac{\vec{C}_{cam} - \vec{P}(i+shear,j)}{\left|\vec{C}_{cam} - \vec{P}(i+shear,j)\right|} \tag{20}$$

The unwrapped phase map for x shear is obtained by equation (3):

$$\Delta\phi(i,j)\Big|_{cam,x} = \frac{2\pi}{\lambda}\vec{k} \cdot \begin{bmatrix} u_2 - u_1 \\ v_2 - v_1 \\ w_2 - w_1 \end{bmatrix} \cong \frac{2\pi}{\lambda}\vec{k}(i,j)\Big|_{cam,x} \cdot \begin{bmatrix} \partial u/\partial x(i,j) \\ \partial v/\partial x(i,j) \\ \partial w/\partial x(i,j) \end{bmatrix} \cdot x_{shear} \tag{21}$$

The phase map for shear in the y direction is obtained using equation (21), but with the displacement gradient and actual shear distance along the y direction. The above implementation causes division followed by multiplication by the actual shear distance. A simplified implementation using equation (22) is also possible. In both cases the results are identical.

$$\Delta\phi(i,j)\Big|_{cam,x} = \frac{2\pi}{\lambda}\vec{k} \cdot \begin{bmatrix} u_2 - u_1 \\ v_2 - v_1 \\ w_2 - w_1 \end{bmatrix} = \frac{2\pi}{\lambda}\vec{k} \cdot \begin{bmatrix} u(i,j) - u(i,j-shear) \\ u(i,j) - u(i,j-shear) \\ u(i,j) - u(i,j-shear) \end{bmatrix} \tag{22}$$

5. SIMULATION RESULTS

5.1 Cylinder sample

The load applied to the cylinder generates spatially constant radial and axial displacements. The tangential displacement is null. When converted to the Cartesian coordinates of figure 6, by following a horizontal path, all displacements tend to maintain a constant value. This explains the lack of fringes in most of the phase map for x shear. For y shear, by following a vertical path, out of plane (z direction) displacements are obtained on the central region and are gradually substituted by in plane displacements. This behavior explains the variation in fringe density on the phase map with y shear. The regions close the end caps show fringe concentrations because these areas present subtle strain variation. Additionally, the end caps were welded to the cylindrical surface thus the accuracy of FE models for these regions is not so high.

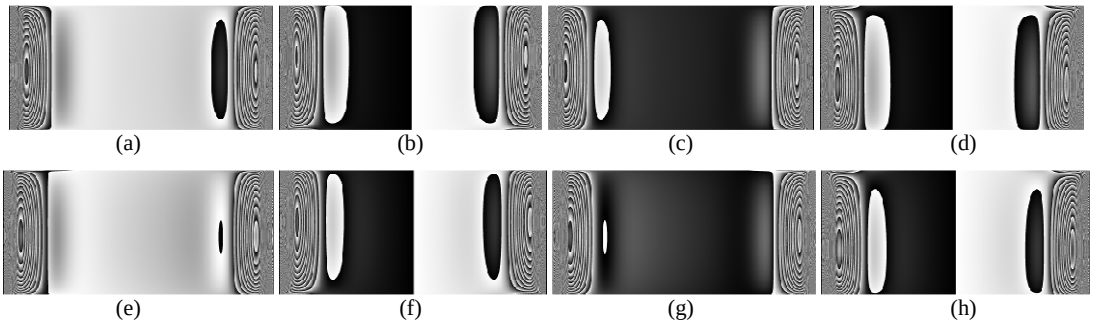

Figure 8. Phase maps of the cylinder sample with 1 mm x shear, obtained by inverted shearography software (a), (b), (c), (d) and by phase length method (e), (f), (g), (h). Phase maps for all the four cameras are shown.

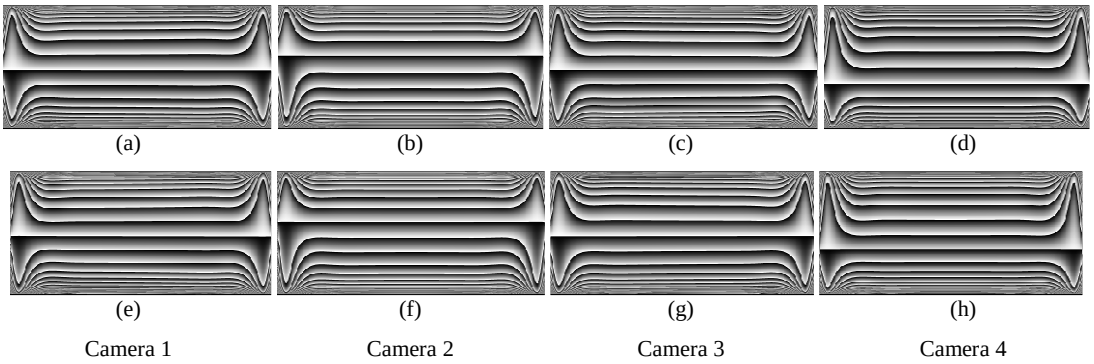

Figure 9. Phase maps from the cylinder sample with 1 mm y shear, obtained by inverted shearography software (a), (b), (c), (d) and by phase length method (e), (f), (g), (h). Phase maps for all the four cameras are shown.

Image perspective distortion due to camera position was not take into account for the simulation, thus the resulting maps of phase change must be seen as images after dewarping to a normal viewing angle, see figure 6. The cameras have different sensitivity vectors, due to their positions, for this reason the phase maps are different for each camera.

The uncertainty due to the material properties, manufacture tolerances and loading inaccuracy is observed in the form of an uncertainty of the phase values ϕ_Δ. Equation (23) is an example showing how the uncertainty map at minimum error limit is calculated.

$$\phi_\Delta(i,j) = \Delta\phi(i,j)\big|_{no\,\min al} - \Delta\phi(i,j)\big|_{\min error\,\lim it} \tag{23}$$

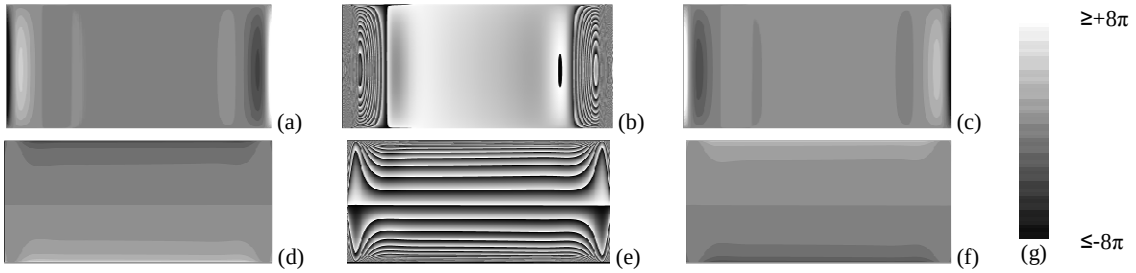

Figure 10. Maps of phase uncertainty ϕ_Δ at minimum (a), (d) and at maximum error (c), (f). Nominal phase maps for camera 1 (b), (e). (a), (b) and (c) are for x shear and (d), (e) and (f) are for the y shear. The scale (g) is valid for the maps of phase uncertainty and each grey level represents a range of 2π radians.

For the central region, the difference between the phase maps at maximum error limit and minimum error limit do not exceed 0,5π radians for x shear and 4π radians for y shear. This difference reaches 20π radians for some points at the edge of the sample.

5.2 Plate sample

Both optical simulation methods generate phase maps with similar fringe shapes but with different fringe density for the same shear distance, cameras and source positions. This effect is difficult to observe on the cylinder sample due to high fringe density, but it becomes clear on the phase maps for the plate sample.

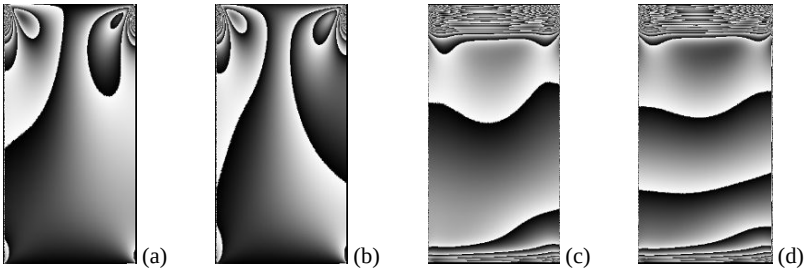
(a) (b) (c) (d)

Figure 11. Phase maps of the plate sample from camera 1 with obtained by the inverted shearography software method with x shear (a) and y shear (c) and by the path length method (b), (d).

The loading causes close to uniform axial strain in the vertical direction. The strain components viewed for the x and z directions are present due to Poisson's effect. An in plane shear strain is expected at all four corners of the sample due to the clamping system. The non-symmetry of the fringes is due to the camera position. These phase maps were also generated for cameras 2, 3 and 4. For cameras 2 and 4 generate symmetric maps are calculated and for camera 3 an asymmetric map that is the mirror of the map from camera 1 is generated. Large strain variation is expected on the bottom and top regions due to the bending effect of the loading and due to the clamping system, which explains the high fringe density obtained on these regions.

The effect of the uncertainty on the material properties, manufacture tolerances and loading inaccuracy is also more apparent for the plate sample. For the central region, the difference between maps of phase change at maximum and minimum error limit does not exceed 4π for both shear directions.

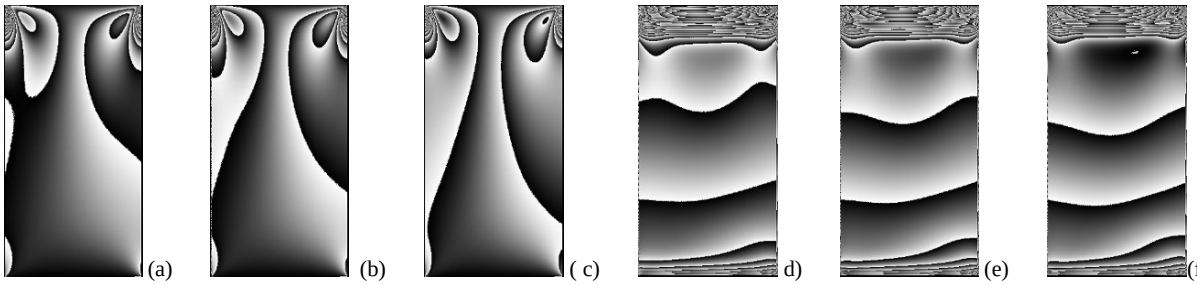
(a) (b) (c) d) (e) (f)

Figure 12. Phase maps from camera 1, obtained by the path length method showing the fringe dislocation due to uncertainties. (a) (b) (c) are maps with x shear at minimum, nominal and maximum error limit respectively and (d), (e), (f) are maps with y shear at minimum, nominal and maximum error limits.

6. DISCUSSION

Although the difference on the unwrapped phase maps is visually not as clear as on the wrapped images due to the absence of fringes, unwrapped maps are suitable for a numeric comparison between the simulation methods. The figures below represent the difference, described by equation (24), between the two simulation methods.

$$difference(i,j) = \frac{\Delta\phi(i,j)\big|_{pathlength} - \Delta\phi(i,j)\big|_{inverted}}{\Delta\phi(i,j)\big|_{pathlength}}, if\ \Delta\phi(i,j)\big|_{pathlength} \neq 0 \qquad (24)$$

(a) (b) (c)

Figure 13. Comparison of unwrapped phase maps from camera 1 for the cylinder sample with x shear (a) and y shear (b). (c) scale where each grey level represents a range of 12,5% of difference.

Regions with sudden error variation between -100% and +100% (indicated by the arrows on figure 13) are associated with areas at zero fringe order, where the phase change values becomes negative. The proximity to zero causes the percentage difference defined by equation (24) to increase significantly.

Equation (2) is the main equation used on path length method. This equation is the starting point to deduce the main equation of the inverse shearography software method, which is equation (3). This deduction involves approximations which tend to be better for higher working distances (here defined as the distance between the origin of the global coordinate system and the cameras along z direction). From this point of view, the difference in the methods is a measurement of the influence of the approximations made for the sensitivity vector.

Simulations were repeated with different working distances but keeping the viewing and illumination angles the same. The improvement of the sensitivity vector approximation with increasing working distance is found from the maximum absolute phase difference between the methods, as described by the equation below:

$$\Delta = \max\left|\Delta\phi(i,j)\big|_{pathlength} - \Delta\phi(i,j)\big|_{inverted}\right| \tag{25}$$

Table 1. Effect of the working distance. The difference between the two simulation methods decreases with increasing work distance for most of the simulation set ups (shear directions and sample).

Plate sample				Cylinder sample			
Work distance	200mm	1000mm	5000mm	Work distance	200mm	1000mm	5000mm
Δ for X shear	30,20	3,32	0,53	Δ for X shear	7,34	1,29	0,22
Δ for Y shear	37,30	9,74	2,03	Δ for Y shear	21,52	36,66	38,27

Real phase maps may differ from the simulated images, as none of the methods described consider the finite size of the camera sensor, the optical path inside the interferometer and the variable shear distance due to the sample curvature as well as shear variation introduced by the Michelson interferometer.

7. CONCLUSIONS

Two simulation approaches for a 3D shearography system have been explained. The first method uses displacement data from the FEM to calculate displacement gradient. Sensitivity vector are calculated and are used to estimate the phase map. The second method uses displacements from the FE model to estimate the object surface position before and after loading. The difference of path length is used to estimate the phase map.

The difference between the methods is seen as a measurement of the influence of the approximations made on the sensitivity vector. For the shearography instrument configuration analyzed on this paper, we found that the approximation causes a difference of 2π (one fringe) on the phase map when a working distance of 200mm is used. The approximation is greatly improved when the working distance is increased as expected from the shearography theory. A comparison of simulation methods with real shearography measurements is the subject of on-going research.

Two test samples, a flat plate loaded axially and a cylinder loaded by internal pressure were simulated. Included errors are associated with the sample's material properties uncertainty, loading inaccuracy and manufacturing tolerances. These uncertainties causes an error of 4π (two fringe) on the central area of the phase maps.

8. ACKNOWLEDGEMENTS

The authors gratefully acknowledge TU Delft for the funding of this project. D. T. Goto would like to thank Professor Armando Albertazzi and his research team from UFSC for the support during this research.

REFERENCES

[1] Steinchen, W. and Yang, L., [Digital Shearography], SPIE Press, Bellingham, Washington, 98227-0010 (2003).
[2] Davis, C. K., "Shearographic and thermographic non-destructive evaluation of the space shuttle structure and thermal protection (TPS) Systems," Proc. SPIE 2945, 36-47 (1996).
[3] Farrant D. I. and Petzing, J. N., "Sensitivity errors in interferometric deformation metrology," Appl. Opt 42:28, 5634-41 (2003).
[4] Wan Abdullah, W. S. and Petzing, J. N., "Development of speckle shearing interferometer error analysis as an aperture function of wave front divergence," J. Mod. Opt.52:11, 1495-10 (2005).
[5] Groves, R. M., "Development of Shearography for Surface Strain Measurement of Non-Planar Objects", PhD Thesis, Cranfield University, Bedford, UK (2001).
[6] Lee, J., Yoon, D, Kim, J. and Vautrin, A., "Investigation of shear distance in Michelson interferometer-based shearography for mechanical characterization," Meas. Sci. Techol. 19, 115303 (2008).
[7] Ng T. W., "Shear measurement in digital speckle shearing interferometry using digital correlation," Opt. Comm. 115 241-244 (1995).
[8] Groves, R. M., James, S. W. and Tatam, R. P., "Strain measurement in curved industrial components using multi-component shearography," Proc. SPIE 4398, 216-224 (2001).
[9] Lee, J., Yoon, D, Kim, J. and Vautrin, A., "Investigation of shear distance in Michelson interferometer-based shearography for mechanical characterization," Meas. Sci. Techol. 19, 115303 (2008).
[10] Picart, P., Pascal, J. C. and Breteau, J. M., "Systematic errors of phase-shifting speckle interferometry," Appl. Opt. 40:13, 2107-16 (2001).
[11] Francis, D., James, S. W. and Tatam, R. P., "Surface strain measurement using multi-component shearography with coherent fibre-optic imaging bundles," Meas. Sci. Technol. 18, 3583-91 (2007).
[12] Dorrio B. V. and Fernandez J. L., "Phase–evaluation methods in whole-field optical measurement techniques," Meas. Sci. Technol. 10, R33-R35 (1999).
[13] James, S. W. and Tatam, R. P., "Time-division multiplexed 3D shearography," Proc. SPIE 3744, 394-403 (1999).
[14] Groves, R. M., James, S. W. and Tatam, R. P., "Multi-component shearography employing four measurement channels," Proc. SPIE 4933, 135-140 (2003).
[15] Budynas, R. G. and Nisbett, K. J., [Shigley's Mechanical Engineering Design], McGraw-Hill, New York, (2006).
[16] Hung, Y. Y. and Liang, C. Y., "Image shearing camera for direct measurement of surface strains," Appl. Opt 18:7, 1046-51 (1979).